Right sizes of nano- and microstructures for high-performance and rigid bulk thermoelectrics

Hongchao Wang[a], Je-Hyeong Bahk[b], Chanyoung Kang[a], Junphil Hwang[a], Kangmin Kim[a], Jungwon Kim[a], Peter Burke[c], John E. Bowers[c], Arthur C. Gossard[c], Ali Shakouri[b], and Woochul Kim[a,1]

[a]School of Mechanical Engineering, Yonsei University, Seoul 120-749, Korea; [b]Birck Nanotechnology Center, Purdue University, West Lafayette, IN 47907; and [c]Materials Department, University of California, Santa Barbara, CA 93106

Edited by Mildred S. Dresselhaus, Massachusetts Institute of Technology, Cambridge, MA, and approved June 13, 2014 (received for review February 26, 2014)

In this paper, we systematically investigate three different routes of synthesizing 2% Na-doped PbTe after melting the elements: (*i*) quenching followed by hot-pressing (QH), (*ii*) annealing followed by hot-pressing, and (*iii*) quenching and annealing followed by hot-pressing. We found that the thermoelectric figure of merit, *zT*, strongly depends on the synthesis condition and that its value can be enhanced to ∼2.0 at 773 K by optimizing the size distribution of the nanostructures in the material. Based on our theoretical analysis on both electron and thermal transport, this *zT* enhancement is attributed to the reduction of both the lattice and electronic thermal conductivities; the smallest sizes (2∼6 nm) of nanostructures in the QH sample are responsible for effectively scattering the wide range of phonon wavelengths to minimize the lattice thermal conductivity to ∼0.5 W/m K. The reduced electronic thermal conductivity associated with the suppressed electrical conductivity by nanostructures also helped reduce the total thermal conductivity. In addition to the high *zT* of the QH sample, the mechanical hardness is higher than the other samples by a factor of around 2 due to the smaller grain sizes. Overall, this paper suggests a guideline on how to achieve high *zT* and mechanical strength of a thermoelectric material by controlling nano- and microstructures of the material.

waste heat recovery | energy harvesting

A thermoelectric (TE) device is a solid-state device that converts heat directly into electricity and vice versa (1–5). As there are no moving parts involved and the device configuration is simple, TE devices have demonstrated long-term reliability in various space missions, usually running for tens of years without maintenance (6). However, they are not yet widely used in many other energy conversion applications on earth mainly due to their low conversion efficiencies. The conversion efficiency of a TE device largely depends on the material properties, i.e., the figure of merit (1, 3), $zT = [S^2/\rho(\kappa_L + \kappa_e)]T$, where T is the absolute temperature, S is the Seebeck coefficient, ρ is the electrical resistivity, and κ_L and κ_e are, respectively, the lattice (or phonon) and electronic thermal conductivities. Increasing the zT has proven challenging because the constituent TE properties are interdependent; for example, decreasing the electrical resistivity results in decreasing the Seebeck coefficient and increasing the electronic thermal conductivity.

Among the various TE materials, PbTe is known to be a very useful TE material for waste heat recovery in the temperature range of 600–900 K (1, 4, 6–8). This material has been used widely since the onset of the Space Age in the late 1950s. According to an excellent review of 20th century TE materials by Wood et al. (7) in 1988, PbTe was the core material used in the first radioisotope TE generator launched into space, called SNAP-3G. SNAP-3G had been operational for more than 26 y without any failures since its launch in 1961 (7). Interestingly, the zT of PbTe was believed to be around 0.7 at 600∼800 K (7). However, according to a later paper by Pei et al. (9), the zT of Na-doped PbTe was found to be as high as ∼1.4 at 750 K after more precise thermal conductivity measurements at high temperatures. Recently, PbTe has been the subject of extensive research involving various new approaches for enhancing the TE properties. These efforts include band convergence via alloys (10) and electronic density of states distortion by resonant levels (11, 12) to enhance the power factor (13, 14), as well as a variety of embedded nanostructures to reduce the thermal conductivity (15–19). Heremans et al. (11, 12) showed that the power factor of PbTe can be enhanced by doping with an appropriate impurity such as Tl, which creates resonant levels inside the electronic band of PbTe. They reported a zT value of 1.5 at 773 K for 2% Tl-doped PbTe. Band convergence has been suggested as another method of increasing the power factor; Pei et al. (10) reported an enhancement of the figure of merit to 1.8 at around 850 K due to an optimized power factor via the convergence of at least 12 valleys in $Pb_{0.98}Na_{0.02}Te_{1-x}Se_x$ alloys. In addition, by tuning the energy separation between the three bands (C + L + Σ) to achieve an optimal carrier concentration in 2 mol % Na-doped $Mg_xPb_{1-x}Te$ alloys (20), a significant enhancement of the zT over a wide temperature range was achieved, with a peak zT value of ∼1.7 at 725 K. It is now well known that nanostructures such as nanoparticles (15–17, 21) and nanosized grain boundaries (18) can scatter phonons effectively, thereby reducing the thermal conductivity. Girard et al. (22) reported that the Na-doped PbTe–PbS 12% formed PbS nanostructures, which reduced the lattice thermal conductivity significantly and thus achieved a maximum zT of 1.8 at 800 K. Recently, a significant enhancement of the figure of merit of 2.2 at 915 K in spark-plasma-sintered (SPS) 2% Na-doped PbTe–SrTe alloys was reported by Biswas et al. (15) These authors attributed the large increase in zT to the thermal conductivity reduction achieved

Significance

PbTe is known to be a promising thermoelectric material for waste heat recovery, so it has been the subject of extensive research involving new approaches. It is important to note that the performances of these developed materials can depend on the material synthesis conditions. We investigated three different routes of synthesizing 2% Na-doped PbTe and found that its thermoelectric figure of merit, *zT*, can be enhanced to ∼2.0 at 773 K. Also, the mechanical hardness of the sample synthesized by this condition was nearly double than that of the other samples. Our study shows that the size of nano- and microstructures can vary significantly by the choice of synthesis methods, which can explain the variation in *zT*s and mechanical hardness.

Author contributions: H.W. designed research; H.W., J.-H.B., C.K., J.H., K.K., J.K., P.B., and W.K. performed research; J.-H.B., J.E.B., A.C.G., A.S., and W.K. analyzed data; and H.W., J.-H.B., and W.K. wrote the paper.

The authors declare no conflict of interest.

This article is a PNAS Direct Submission.

[1]To whom correspondence should be addressed. Email: woochul@yonsei.ac.kr.

This article contains supporting information online at www.pnas.org/lookup/suppl/doi:10.1073/pnas.1403601111/-/DCSupplemental.

by "all-scale hierarchical architectures," which cause extensive phonon scattering over a broad range of phonon wavelengths with structures of various length scales, i.e., atomic-scale impurities for scattering short-wavelength phonons, nanoscale precipitates for midwavelength phonons, and mesoscale grains for long-wavelength phonons.

The performances of these recently developed nanostructured TE materials can depend heavily on the material synthesis method and conditions used; their enhanced TE properties largely depend on the micro- and nanostructures in the materials, which can be significantly altered by small changes in the synthesis conditions. Despite recent extensive research on PbTe and its alloys, however, the effects of different synthesis methods and conditions on their TE properties have been neglected in the research thus far. In this paper, we systematically investigate three different routes of synthesizing 2% Na-doped PbTe to study their effects on the TE properties. After melting the elements, three different material synthesis routes are used: (*i*) quenching followed by hot-pressing (QH), (*ii*) annealing followed by hot-pressing (AH), and (*iii*) quenching and annealing followed by hot-pressing (QAH). We compare the TE properties of the samples synthesized by these three methods and investigate the variation of the nanostructures and grain sizes in the samples using scanning electron microscopy (SEM) and transmission electron microscopy (TEM). It was found that the zT strongly depends on the synthesis condition and that its value can be enhanced from 1.5∼1.7 (AH, QAH) to 2.0 or higher (QH) at 773 K. Based on a theoretical analysis of both electron and thermal transport, we attribute this zT enhancement to the reduction of both the lattice and electronic thermal conductivities; we found that the sizes of the nanoscale precipitates and microscale grains vary significantly among the samples when different synthesis methods are used. Our theoretical analysis reveals that this clearly affects the TE properties of the samples. In particular, QH showed the smallest sizes of both the precipitates and the grains, thus exhibiting a zT of 2.0 at 773 K. We also tested the hardness of the samples, which is important for mechanical stability in practical applications. The hardness of the QH samples was the highest among all samples and was nearly double that of the QAH samples.

Results and Discussion

Based on the powder X-ray diffraction (XRD) pattern for the three $Pb_{0.98}Na_{0.02}Te$ samples synthesized by the three different processes of QH, AH, and QAH (shown in Fig. S1), we confirmed that the XRD patterns of the three samples are fairly similar to one another in the measured angle range. All of the typical peaks of the three samples can be indexed to the face-centered-cubic rock-salt structure. We obtained SEM images to determine the morphological differences among the three different samples (Fig. 1 *A–F*). All of the figures are cross-sectional images. In the low-magnification images (Fig. 1 *A–C*), it is clearly observed that the grain sizes are homogeneous in the AH sample, with an average grain size of ∼100 μm (Fig. 1*A*). On the other hand, in the QH sample, although the grain sizes are generally homogeneous, their average size (around 5 μm) is much smaller than that of the AH samples (Fig. 1*C*). Interestingly, these two different length scales of grains coexist in the QAH sample (Fig. 1*B*). This can be observed more clearly in the high-magnification SEM images shown in Fig. 1 *D–F*. The grain boundaries are clearly shown in the figures, and the grains are closely packed with almost no voids between them. In general, the AH grain sizes are fairly large, such that whole grains cannot be captured in the low-magnification SEM image (Fig. 1*D*), although few smaller grains are observed in the grain boundaries. Smaller grains in the QAH (Fig. 1*E*) and grains in the QH (Fig. 1*F*) samples are clearly observable in the images. This result may be attributed to the insufficient time for the grain to grow larger in the QH sample due to the quenching process, whereas sufficient time was given, along with sufficient atomic kinetics, during the annealing process for small grains to grow into much larger grains in the AH and QAH samples. Therefore, small grains ∼5 μm in size on average could be formed by the quenching process, whereas larger grains ∼100 μm in size are grown during the annealing process. TEM images of the samples are shown in Fig. 1 *G–L*. The TEM sample was prepared by a focused ion beam, and the thickness variation should therefore be negligible. In the high-magnification TEM images (Fig. 1 *G–I*), nanostructures with different sizes depending on the synthesis method, i.e., QH, QAH, or AH, are clearly shown. This is consistent with recent reports by He et al. (23, 24) in which Na precipitates in 2% Na-doped PbTe were observed, as the sodium content exceeded the solubility limit (0.5 mol %) of the Na in the PbTe. The 0.5% sodium content, below the solubility limit, introduces point defects (solid solution formation) in PbTe, and the remainder would precipitate as nanostructures. This solubility limit of 0.5 mol % was later confirmed by Yamini et al. (25) in their study on the temperature-dependent solubility of Na in the PbTe. They also showed that the additional Na in PbTe beyond the solubility limit induces the formation of a Na-rich liquid phase at temperatures above 633 K at grain boundaries. Magnified images of the nanostructures are provided in Fig. 1 *J–L*. Although these nanostructures are coherent, the shapes are quite different; whereas a spherical shape with a diameter of a few nanometers is observed for QH; irregular shapes are shown in the QAH and

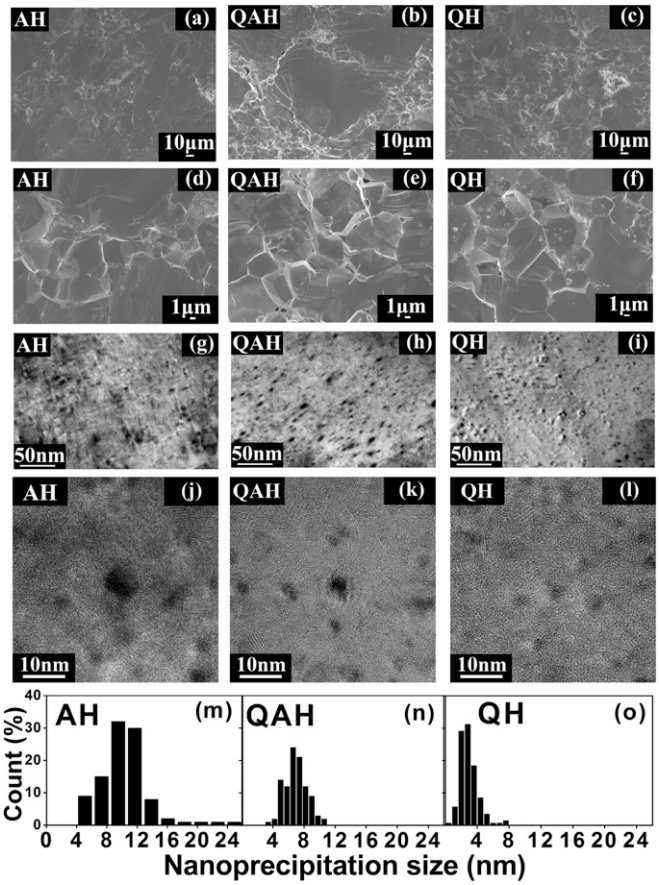

Fig. 1. SEM and TEM images of the $Pb_{0.98}Na_{0.02}Te$ samples. Low- (*A–C*) and high- (*D–F*) magnification SEM images of the QH, AH, and QAH (27) samples showing microsized grains. Nanostructures of different sizes are observed in the low- (*G–I*) and high- (*J–L*) magnification TEM images. The sizes of these nanostructures are quantified and presented in *M–O*.

AH results. The spherical nanostructures may have agglomerated during the annealing process. A similar finding was reported by Lensch-Falk et al. (26) in their study on Ag_2Te precipitates in a PbTe matrix; they found that Ag_2Te precipitates form as coherent spherical nanoparticles in the quenched sample, yet these evolve into flattened semicoherent disks in the annealed samples. The sizes of these nanostructures are quantified and shown in Fig. 1 *M–O*. The mean size of the AH sample is the largest, and that of the QH sample is the smallest. The mean size of QAH sample is between these values, but it is more toward the AH size. Also, the distribution of the sizes in the AH set is the largest. As expected, quenching is a very effective means of forming smaller nanostructures, whereas annealing makes them grow into larger structures.

The temperature-dependent figures of merit for the QH, AH, and QAH samples are presented in Fig. 2. In addition, schematics of their nano- and microstructures are shown. The zT value for the QH sample at each temperature is the average value of 13 measurements. Error bars indicate deviations in the zT measurements. It was predicted in a previous report (10) that an optimized zT in heavily doped p-type PbTe could be as high as 1.7 at 750 K based on a model that takes multiple bands into account. However, the zT of our QH sample is even higher than that, reaching ~2.0 at 773 K. On the other hand, the AH and QAH samples had zT values of ~1.5 and 1.6, respectively, at 773 K, which is lower than that of the QH sample at the same temperature. Our theoretical analysis, explained later in this paper, revealed the following: At high temperature, the power factor of QH sample is around 4% higher than that of QAH sample, yet the thermal conductivity of QH is around 14% lower than that of the QAH. Also, even though the electrical resistivity of QH sample is lower than that of QAH, i.e., higher electronic thermal conductivity of QH over that of QAH, the total thermal conductivity of QH is lower than that of QAH. This clearly indicates the lattice thermal conductivity of QH is lower than that of QAH. The theoretical analysis reveals that the smaller sizes of nanostructures in QH samples led to reduced interparticle spacing in nanostructures which effectively scattered phonons. For comparison, we also plotted in Fig. 2 previously reported zT values of PbTe:Na (9, 15). Pei et al. (9) synthesized PbTe:Na by melting–quenching–annealing followed by a hot-pressing process similar to our QAH process. The zT value for this reference material is ~1.4 at a temperature of ~750 K, which is slightly lower than the zT of our QAH. This may have arisen because our QAH sample was synthesized based on an optimized hot-pressing condition (27). In addition, Biswas et al. (15) synthesized PbTe:Na via melting–quenching followed by an SPS process and reported a zT close to 1.4 at 800 K. We suspect that a different synthesis process might have caused this deviation. Furthermore, it is known that an alkali-doped (2P) material has poorer mechanical properties (28). However, in our mechanical hardness analysis, shown in Fig. 2 (*Inset*), the hardness of the QH sample is nearly double that of the QAH sample. The mechanical hardness was measured by a Zwick μ-S Vickers hardness tester. These values are based on the average of five measurements each. It is known (29) that the hardness increases as the grain size becomes smaller, given that a smaller grain restricts slip and dislocation (30).

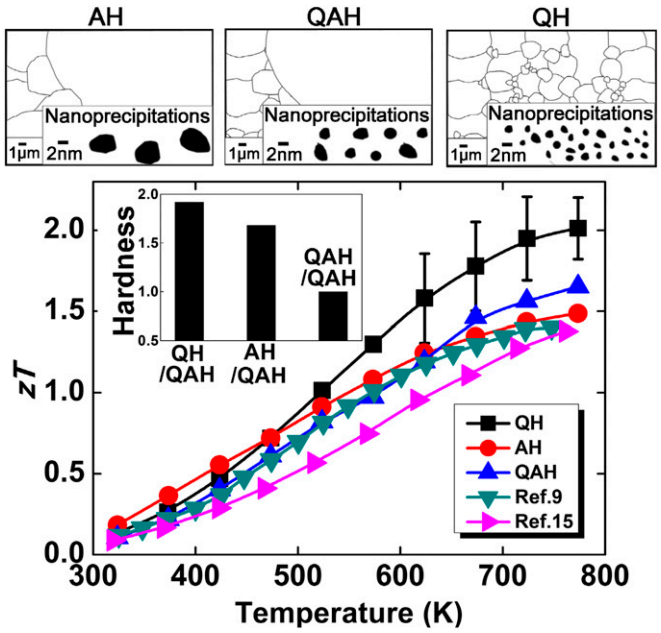

Fig. 2. TE figures of merits for the QH, AH, and QAH samples with other reference data (9, 15). The zT values of the QH sample are based on the average values of 13 measurements. The error bar indicates the highest and the lowest zT values in the measurements. The schematics of morphologies of the sample are also shown. (*Inset*) Normalized mechanical hardness of the QH, AH, and QAH samples.

The electrical resistivities, Seebeck coefficients, and power factors of the three samples are presented as a function of the temperature in Fig. 3. Along with the experimental data, the theoretical calculations for bulk p-type PbTe are plotted in the figure. Details regarding the theoretical transport modeling can be found in *SI Text*. The electrical resistivities for all three samples increase with an increase in the temperature, as similarly occurs in metals. The difference as regards metals is that the hole concentration increases with the temperature in all of the samples, as evidenced by the Hall effect measurement results shown in Fig. S2. According to earlier work (ref. 15), the sodium atoms trapped at the grain boundaries cannot donate carriers to the matrix. However, these sodium atoms diffuse into the matrix as the temperature rises, becoming electrically active to provide more carriers at a higher temperature. The AH sample had a lower hole concentration (3.5×10^{19} cm^{-3}) compared with the QAH and QH samples (5.0×10^{19} cm^{-3} and 6.5×10^{19} cm^{-3}, respectively) at room temperature, but it increased more rapidly with the temperature than the others, particularly at high temperatures above 600 K, such that the AH sample showed a slight decrease in its resistivity when the temperature exceeded 650 K despite the fact that the mobility decreases with the temperature due to the increased acoustic phonon scattering. This is consistent with the theoretical calculations shown in Fig. 3*A*. The higher experimental resistivity compared with the calculation for all of the samples is believed to be due to additional carrier scattering by the grain boundaries and nanostructures in the material, although this was not included in the modeling.

The Seebeck coefficient also increases with an increase in the temperature for all of the samples, but it becomes saturated at 250~300 μV/K above 650 K. Typically, the Seebeck coefficient tends to increase steadily with the temperature at a constant carrier concentration. However, in these samples, the hole concentration rapidly increases with the temperature at high temperatures above 650 K, which prevents the Seebeck coefficient from increasing further. The QH sample had the highest hole concentration (~1.0×10^{20} cm^{-3} at 773 K) among the three samples over the entire temperature range, although it is not much different from that of the QAH sample. Therefore, the QH sample has the lowest Seebeck coefficient and lowest resistivity among them. The reason for the variation in hole concentration among the samples is not yet clearly understood, but it may be related to the densities of the defects and/or electrically active impurities such as Na in the matrix.

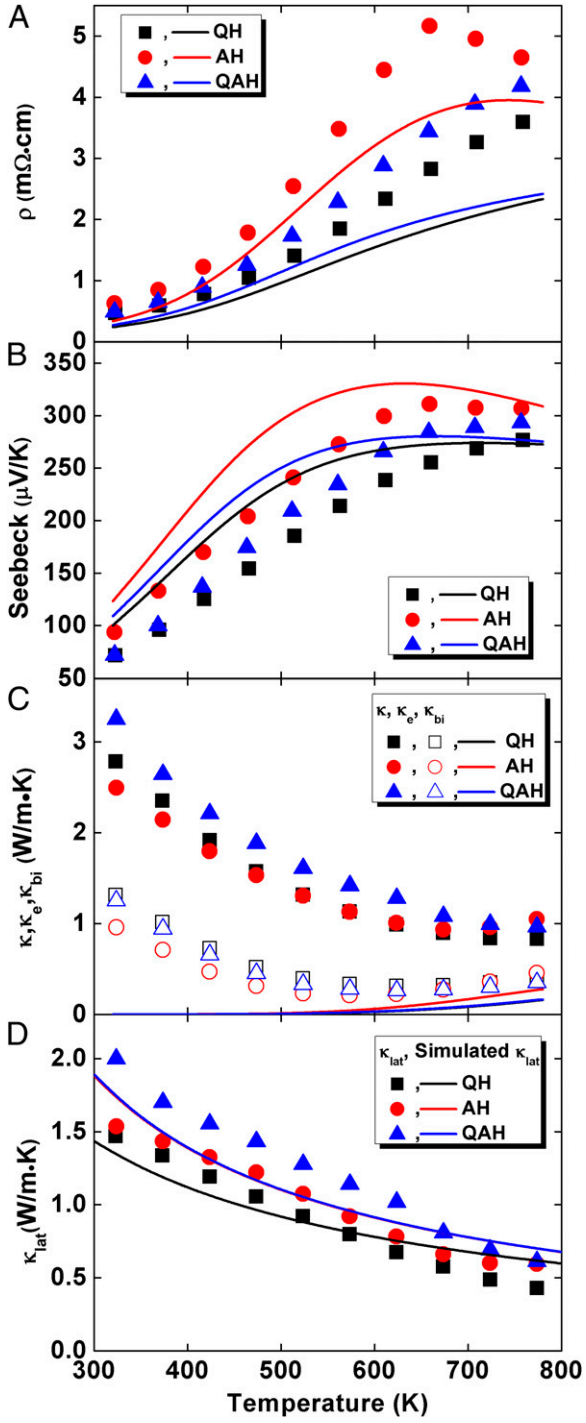

Fig. 3. TE properties of the QH, AH, and QAH samples: (*A*) electrical resistivities; (*B*) Seebeck coefficients; (*C*) the total electronic and bipolar thermal conductivities; and (*D*) the lattice thermal conductivities. The dots indicate the experimental data, and the line denotes the theoretical analysis data.

Fig. 3*C* shows the measured total thermal conductivity (κ) along with the calculated electronic and bipolar thermal conductivities for the three samples. The electronic thermal conductivity (κ_e) includes the bipolar thermal conductivity (κ_{bi}), and it is used to extract the lattice thermal conductivity via $\kappa_l = \kappa - \kappa_e$. More details about the bipolar thermal conductivity calculation are found in *SI Text*. The electronic thermal conductivity before the bipolar term is included is calculated by the Wiedemann–Franz law as $\kappa_e - \kappa_{bi} = LT/\rho$, where L is the Lorenz number. The Lorenz number is calculated from the multiband Boltzmann transport model described in *SI Text*. As the Lorenz number remains almost constant for all three samples at a given temperature, as shown in Fig. S3*A*, the electronic thermal conductivity without the bipolar term is largely determined by the resistivity. As shown in Fig. 3*C*, bipolar thermal conductivity starts to appear beyond 600 K in all three samples, becoming as large as 0.27 W/m K at 773 K for the AH sample. The QH and QAH samples have bipolar thermal conductivity of ∼0.15 W/m K at the same temperature, which is lower than that of the AH sample due to their relatively higher hole concentrations compared with the AH sample, which lowers the contribution from the electrons to the bipolar thermal conductivity. As a result, the AH sample has higher electronic thermal conductivity (∼0.46 W/m K at 773 K) than the QH (0.4 W/m K) and QAH (0.36 W/m K) samples, although it has the highest resistivity among the samples. The large bipolar thermal conductivity of the AH sample is responsible for the slight increase in the measured total thermal conductivity at high temperatures beyond 750 K for the AH sample, as shown in Fig. 3*C*.

The lattice thermal conductivity κ_L is then obtained by subtracting the electronic thermal conductivity from the total thermal conductivity, as shown in Fig. 3*D*. To understand why the QH exhibited the lowest thermal conductivities among the samples, we used the Callaway model (31). A detailed analysis is available in *SI Text*, and the results are presented as solid curves in Fig. 3*D*. We reflected in the simulation what we observed in the SEM and TEM images (Fig. 1). First, we set the size of the grain to be 100, 8, and 3.7 μm for the AH, QAH, and QH samples, respectively, based on the SEM images in Fig. 1. Also, based on findings by He et al. (23), the solubility limit of Na in PbTe is 0.5%. The remaining 1.5% should be precipitated, although the exact amount of this should be varied among samples due to the different synthesis condition, measurement history, sample variation, etc. Based on the SEM and TEM images, we assumed that the remaining 1.5% was precipitated in the form of Na_2Te, with a diameter of around 10, 7, and 2.4 nm for the AH, QAH, and QH samples, respectively. However, the solubility limit of Na atoms in PbTe can increase as temperature increases (25), which can be the reason that the carrier concentration increases with temperature due to the further diffusion of Na atoms into the matrix at higher temperatures. This may affect the size distribution of the nanoprecipitates at high temperatures, which is subject to future study. As shown in Fig. 3*D*, incorporation of these values indeed explains why the QH sample has the lowest thermal conductivity. In the simulation, lattice thermal conductivities of QAH and AH are similar despite the fact that they have different grain sizes and diameters of their nanostructures. It is known that phonon grain boundary scattering is usually dominant at temperatures lower than the Debye temperature (32) unless the sizes of the grains are very small, e.g., on the order of a few tens of nanometers (16). Considering that the Debye temperature of PbTe (33) is 136 K, the differences in the grains did not affect the lattice thermal conductivities significantly in the measured temperature range. Thus, scattering due to the nanostructures indeed causes this discrepancy. In fact, given that we fixed the concentration of the nanostructures at 1.5%, the differences in the diameters of the nanostructures, which effectively scatter mid- to long-wavelength phonons (17), affected the lattice thermal conductivities. It is known (34) that, given the same nanostructure concentration, the mean size of the nanostructure is directly related to the interparticle spacing assuming homogeneous distribution of nanostructures; the smaller the size of the nanostructure, the closer the interparticle spacing. The spacings between the nanostructures could be estimated as 22.7, 15.8, and 5.4 nm for the AH, QAH, and QH samples, respectively. This suggests that the phonon

mean-free path of scattering processes other than scattering due to the nanostructures should be shorter than 15.8 nm because the lattice thermal conductivities of QAH and AH do not appreciably depend on the sizes of the nanostructures. Lattice thermal conductivities of the QH, AH, and QAH samples with and without nanoparticles (NP) were calculated as shown in Fig. S4. It is clear in the figure that effects of NPs on the lattice thermal conductivities are evident in the QH but are negligible in the others. This clearly suggests that, given the same nanostructure concentration, the sizes of the nanostructures are closely related to the interparticle spacing which affects the phonon mean-free path (35).

Conclusions

We demonstrated a zT of ~2.0 at 773 K in Na-doped PbTe in one of the synthesis methods, (QH), used in this paper. Based on our theoretical analysis, the main reason for such a high zT in QH is the reduction of the thermal conductivity. Interestingly, although the microsized grains and nanostructures occur in all three samples, QH, AH, and QAH, nanostructures only a few nanometers in diameter present in QH effectively reduced the lattice thermal conductivity. Based on this finding, we should emphasize that nanostructures are not always effective in reducing the lattice thermal conductivity. They are the most effective when the spacing between them is smaller than the phonon mean-free paths of other scattering processes. Therefore, optimal synthesis condition should be sought to find the right sizes of nanostructures for this material. Our study shows that the size of nanostructures can vary significantly by the choice of synthesis methods and parameters, which can explain the variation in zTs among the samples from different synthesis methods. In addition to the high zT, the QH sample possesses mechanical hardness superior to that of the other samples by a factor of 2. This is due to the relatively small grain sizes compared with the others (29, 30). Overall, this QH sample demonstrates great potential for vehicle waste heat recovery not only due to its high TE figure of merit but also due to its high mechanical hardness for practical use.

Materials and Methods

Materials. $Pb_{0.98}Na_{0.02}Te$ was synthesized by the three different synthesis processes of QH, AH, and QAH. Elemental lead, tellurium, and sodium were used as the starting materials. They were weighted and mixed in a carbon-coated quartz tube under a N_2-filled glove box. The tube was then evacuated and sealed. The elements were heated at 1,073 K for 2 h followed by melting at 1,273 K for 6 h. The ingots were then prepared by the following three different processes: (*i*) The QH sample was obtained by quenching in cold water followed by hot-pressing. (*ii*) For the AH sample, after the melting process, the sample was annealed at 973 K for 2 d in a furnace. After this process, the sample was cooled naturally to room temperature in the furnace, after which it was hot-pressed. (*iii*) For the QAH sample, the melted sample was quenched into cold water. The ingot formed in this way was placed into another carbon-coated quartz tube and was annealed at 973 K for 2 d. The sample was then cooled to room temperature. The QAH sample was obtained after hot-pressing this ingot. In all three processes, the resulting ingot was then ground into powder and subsequently hot-pressed in a uniaxial hot-pressing machine at 100 MPa at 773 K for 1 h, which was found to be the optimal condition for hot-pressing in our previous work (27). Electrical heaters supplied heat in the hot-pressing machine. Details regarding material synthesis can be found in *Supporting Information*.

Thermoelectric Properties. The electrical resistivity and Seebeck coefficient were measured simultaneously over the temperature range between 300 and 800 K using a commercial ULVAC ZEM-3 system. The thermal diffusivity was measured using a laser flash apparatus (Netzsch LFA 457; see Fig. S5). The heat capacity was estimated by the relationship of C_p (k_B per atom) = $3.07 + 4.7 \times 10^{-4} \times (T/K - 300)$, which was obtained by fitting the data to the experimental data reported by Blachnik and Igel (36). The thermal conductivity (κ) was extracted from the thermal diffusivity (λ), the specific heat capacity (C_p), and the density (d) based on the relationship $\kappa = \lambda C_p d$. Here, d was measured by the Archimedes method. The figure of merit was then obtained from the transport property measurements above. We only measured samples with a relative density (see Table S1). Details of other characterization tools used here, such as the mechanical hardness, XRD, and Hall measurements, the theoretical transport modeling, etc. are available in *SI Text*. Specially, sensitivity analysis on lattice thermal conductivity regarding the variation of sizes of nanoparticles and microsized grains is provided in Fig. S6, and the repeated thermoelectric properties of the QH samples are shown in Fig. S7. Additionally, Fig. S8 shows the thermoelectric properties, measured a few months after the synthesis, for QH while heating and cooling the sample.

ACKNOWLEDGMENTS. We thank Hee Jin Kim (Ewha Womans University) for the TEM measurements and Dr. Sudong Park (Korea Electrotechnology Research Institute) for useful discussions. This work was supported by the Mid-career Researcher Program (2011-0028729) and Nano-Material Technology Development Program (Green Nano Technology Development Program) (2011-0030146) through a National Research Foundation of Korea Grant funded by the Ministry of Education, Science and Technology; and an Energy Efficiency and Resources Program of the Korea Institute of Energy Technology Evaluation and Planning Grant funded by the Korean Government Ministry of Knowledge Economy (20112010100100). We also thank the Center for Energy Efficient Materials, an Energy Frontier Research Center funded by the US Department of Energy, Office of Basic Energy Sciences (Award DE-SC0001009) for financial support of P.B., A.S., J.E.B., A.C.G., and W.K.

1. Bell LE (2008) Cooling, heating, generating power, and recovering waste heat with thermoelectric systems. *Science* 321(5895):1457–1461.
2. Majumdar A (2004) Materials science. Thermoelectricity in semiconductor nanostructures. *Science* 303(5659):777–778.
3. Rowe DM (2006) CRC Handbook of Thermoelectrics: Macro to Nano (CRC/Taylor and Francis, Boca Raton, FL).
4. Shakouri A (2011) Recent developments in semiconductor thermoelectric physics and materials. *Annu Rev Mater Res* 41(1):399–431.
5. Snyder GJ, Toberer ES (2008) Complex thermoelectric materials. *Nat Mater* 7(2): 105–114.
6. LaLonde AD, Pei Y, Wang H, Jeffrey Snyder G (2011) Lead telluride alloy thermoelectrics. *Mater Today* 14(11):526–532.
7. Wood C (1988) Materials for thermoelectric energy conversion. *Rep Prog Phys* 51(4): 459–539.
8. Androulakis J, et al. (2010) Thermoelectric enhancement in PbTe with K or Na codoping from tuning the interaction of the light- and heavy-hole valence bands. *Phys Rev B* 82(11):115209.
9. Pei Y, LaLonde A, Iwanaga S, Snyder GJ (2011) High thermoelectric figure of merit in heavy hole dominated PbTe. *Energy Environ Sci* 4(6):2085–2089.
10. Pei Y, et al. (2011) Convergence of electronic bands for high performance bulk thermoelectrics. *Nature* 473(7345):66–69.
11. Heremans JP, et al. (2008) Enhancement of thermoelectric efficiency in PbTe by distortion of the electronic density of states. *Science* 321(5888):554–557.
12. Heremans JP, Wiendlocha B, Chamoire AM (2012) Resonant levels in bulk thermoelectric semiconductors. *Energy Environ Sci* 5(2):5510–5530.
13. Bahk JH, et al. (2011) Thermoelectric power factor enhancement by ionized nanoparticle scattering. *Appl Phys Lett* 99(7):072118.
14. Bahk JH, Santhanam P, Bian ZX, Ram R, Shakouri A (2012) Resonant carrier scattering by core-shell nanoparticles for thermoelectric power factor enhancement. *Appl Phys Lett* 100(1):012102.
15. Biswas K, et al. (2012) High-performance bulk thermoelectrics with all-scale hierarchical architectures. *Nature* 489(7416):414–418.
16. Kang C, Kim H, Park SG, Kim W (2010) Comparison of thermal conductivity in nanodot nanocomposites and nanograined nanocomposites. *Appl Phys Lett* 96(21):213114.
17. Kim W, et al. (2006) Thermal conductivity reduction and thermoelectric figure of merit increase by embedding nanoparticles in crystalline semiconductors. *Phys Rev Lett* 96(4):045901.
18. Poudel B, et al. (2008) High-thermoelectric performance of nanostructured bismuth antimony telluride bulk alloys. *Science* 320(5876):634–638.
19. Pei Y, Heinz NA, LaLonde A, Snyder GJ (2011) Combination of large nanostructures and complex band structure for high performance thermoelectric lead telluride. *Energy & Environmental Science* 4(9):3640–3645.
20. Pei Y, et al. (2011) Stabilizing the optimal carrier concentration for high thermoelectric efficiency. *Adv Mater* 23(47):5674–5678.
21. Hsu KF, et al. (2004) Cubic AgPb(m)SbTe(2+m): Bulk thermoelectric materials with high figure of merit. *Science* 303(5659):818–821.
22. Girard SN, et al. (2011) High performance Na-doped PbTe-PbS thermoelectric materials: Electronic density of states modification and shape-controlled nanostructures. *J Am Chem Soc* 133(41):16588–16597.
23. He J, et al. (2013) Role of sodium doping in lead chalcogenide thermoelectrics. *J Am Chem Soc* 135(12):4624–4627.
24. He J, Androulakis J, Kanatzidis MG, Dravid VP (2012) Seeing is believing: Weak phonon scattering from nanostructures in alkali metal-doped lead telluride. *Nano Lett* 12(1):343–347.

25. Yamini SA, et al. (2013) Rational design of p-type thermoelectric PbTe: Temperature dependent sodium solubility. *Journal of Materials Chemistry A* 1(31): 8725–8730.
26. Lensch-Falk JL, Sugar JD, Hekmaty MA, Medlin DL (2010) Morphological evolution of Ag2Te precipitates in thermoelectric PbTe. *J Alloys Compd* 504(1):37–44.
27. Wang H, et al. (2013) Large enhancement in the thermoelectric properties of $Pb_{0.98}Na_{0.02}Te$ by optimizing synthesis condition. *J Mater Chem A* 1:11269v.
28. Skrabek EA, Trimmer DS (1995) Properties of the general TAGS system. *CRC Handbook of Thermoelectrics*, ed Rowe DM (CRC, Boca Raton, FL), p 272.
29. Callister WC, Rethwisch DG (2012) *Fundamentals of Materials Science and Engineering: An Integrated Approach* (Wiley, New York).
30. van Vlack LH (1973) *A Textbook of Materials Technology* (Addison-Wesley, Reading, MA).
31. Callaway J (1959) Model for lattice thermal conductivity at low temperatures. *Phys Rev* 113(4): 1046–1051.
32. Tien CL, Majumdar A, Gerner FM (1998) *Microscale Energy Transport* (Taylor & Francis, Washington, DC).
33. Lo SH, He JQ, Biswas K, Kanatzidis MG, Dravid VP (2012) Phonon scattering and thermal conductivity in p-type nanostructured PbTe-BaTe bulk thermoelectric materials. *Adv Funct Mater* 22(24):5175–5184.
34. Kim W (2005) *Thermal Transport in Nanostructured Materials* (Univ of California, Berkeley Press, Berkeley, CA).
35. Pei Y, LaLonde AD, Heinz NA, Snyder GJ (2012) High thermoelectric figure of merit in PbTe alloys demonstrated in PbTe–CdTe. *Adv Energy Mater* 2(6):670–675.
36. Blachnik R, Igel R (1974) Thermodynamic properties of IV-VI-compounds - lead - chalcogenides. *Z Naturforsch B* 29:625–629.

Supporting Information

Wang et al. 10.1073/pnas.1403601111

SI Text

Synthesis. $Pb_{0.98}Na_{0.02}Te$ samples were synthesized by three different synthesis processes: quenching followed by hot-pressing (QH); annealing followed by hot-pressing (AH); quenching and annealing followed by hot-pressing (QAH). Elemental lead (Pb, 3N, Alfa Aesar), tellurium (Te, 4N, Alfa Aesar), and sodium (Na, 99.95%, Alfa Aesar) were used as the starting materials. They were weighted in a stoichiometric proportion and mixed in a carbon-coated quartz tube under a N_2-filled glove box. The tube was then evacuated to $\sim 10^{-4}$ torr and sealed. They were heated to 1,073 K for 2 h followed by melting at 1,273 K for 6 h. In the following process, the ingots were prepared by three different synthesis processes: (*i*) the QH sample was obtained by quenching in cold water followed by hot-pressing at 100 MPa at 773 K for 1 h. (*ii*) For the AH sample, after the melting process, the sample was slowly cooled from 1,273 to 973 K at a cooling rate of 300 K/h. The sample was then soaked at the annealing temperature, 973 K, for 2 d in a furnace. After this, the sample was cooled naturally to room temperature in the furnace. The sample was then hot-pressed under the same condition used in the QH process. (*iii*) For the QAH sample, the melted sample was quenched into cold water. The ingot formed in this way was placed into another carbon-coated quartz tube and heated to 973 K for 2 d. The sample was then cooled to room temperature. The QAH sample was obtained after hot-pressing this ingot. In all three different processes, the same hot-pressing condition was used based on the optimized condition for this material obtained from our previous work (1).

Characterization. The crystal structures of the samples were characterized by powder X-ray diffraction (XRD) with Cu Kα radiation at room temperature using a Rigaku powder X-ray diffractometer. The cross-sectional morphology was obtained by a JSM-6701F scanning electron microscope (SEM). Transmission election microscopy (TEM) was carried out using a JEM-2100F microscope. The thin TEM specimen was prepared by a focused ion beam with a condition suggested by Baram and Kaplan (2). The electrical resistivities and Seebeck coefficients were measured simultaneously over the temperature range of 300 to 800 K using an ULVAC ZEM-3 instrument in a helium atmosphere. The carrier concentration was determined by temperature-dependent Hall coefficient measurements. The thermal diffusivity was measured with a laser flash apparatus (Netzsch LFA 457) as shown in Fig. S1. The heat capacity was estimated by the relationship C_p (k_B per atom) = $3.07 + 4.7 \times 10^{-4} \times (T/\mathrm{K} - 300)$, as obtained by fitting the data to the experimental data reported by Blachnik and Igel (3). The thermal conductivity κ was extracted from the thermal diffusivity (λ), the specific heat capacity (C_p), and the density (d) based on the relationship $\kappa = \lambda C_p d$. Here, d is measured by the Archimedes method. The figure of merit was then obtained from the transport property measurements above. The mechanical hardness was measured by a Zwick μ-S Vickers hardness tester.

Power XRD. The powder XRD patterns for the three $Pb_{0.98}Na_{0.02}Te$ samples synthesized by the three different processes, QH, AH, and QAH, are shown in Fig. S2. XRD patterns of the three samples are similar to one another in the measured angle range. As shown in the figure, all typical peaks of the three samples can be indexed to the face-centered-cubic rock-salt structure. We confirmed that the PbTe belongs to the *Fm-3m* space group and did not observe Na or other phases within the detection limits of XRD. The lattice constants, volumes, theoretical densities calculated from XRD data, and experimental densities are shown in Table S1.

Electron Transport Modeling for Bulk PbTe. PbTe is a semiconductor with a relatively large band gap, having a 320-meV band gap at room temperature. A direct band gap is located at the L valley in the Brillouin zone, and another valence band at the Σ-valley has its band maximum close to that of the L-valley valence band with ~40-meV energy spacing (4). The band gap remains almost constant at ~360 meV at temperatures higher than 400 K, as the second valence band at the Σ-valley of 12 degeneracy becomes the primary beyond ~550 K, whereas the L-valley valence band steadily decreases in energy as the temperature moves away from the conduction band minimum (5). Our transport model is based on the linearized Boltzmann transport equation with an approximate relaxation time. All of the transport properties are expressed as integral functions of the differential conductivity $\sigma_d(E)$ over energy E, defined as

$$\sigma_d(E) = e^2 \tau(E) v_x^2(E) \rho_{DOS}(E) \left(-\frac{\partial f_0(E)}{\partial E} \right), \qquad [S1]$$

where e is the electron charge, τ is the relaxation time, ρ_{DOS} is the density of states, v is the carrier velocity, and f_0 is the Fermi–Dirac distribution. For the multiple-band transports in PbTe, the transport properties are calculated in each of the bands with the relative position of the Fermi level E_F from the band extremum and the contributions from each band are then added together to find the total transport values in the bulk. The electrical conductivity σ, the Seebeck coefficient S, and the Lorenz number L are given, respectively, by

$$\sigma = \sum \int \sigma_d(E) dE, \qquad [S2]$$

$$S = \sum \left(\frac{k_B}{q} \right) \int \left[\frac{(E - E_F)}{k_B T} \right] \frac{\sigma_d(E)}{\sigma} \, dE, \qquad [S3]$$

and

$$L = \sum \frac{1}{\sigma} \left(\frac{k_B}{q} \right)^2 \int \left[\frac{E - E_F}{k_B T} \right]^2 \sigma_d(E) dE - S^2, \qquad [S4]$$

where Σ is the sum over the bands, q is $-e$ for the conduction bands and $+e$ for the valence bands, T is the absolute temperature, and E_F is the Fermi energy. The electrical resistivity ρ is the reciprocal of the electrical conductivity such that $\rho = 1/\sigma$.

As shown in Fig. S3*A*, the Lorenz number almost linearly decreases from $2.0 \times 10^{-8} \cdot \mathrm{W}\,\Omega^{-1} \cdot \mathrm{K}^{-2}$ to $1.05 \times 10^{-8} \cdot \mathrm{W}\,\Omega^{-1} \cdot \mathrm{K}^{-2}$ as temperature increases from 300 to 500 K, after which it increases slightly with the temperature to reach $1.15 \sim 1.18 \times 10^{-8} \cdot \mathrm{W}\,\Omega^{-1} \cdot \mathrm{K}^{-2}$ at 780 K for a wide range of hole concentrations between $0.4 \sim 1.5 \times 10^{20}$ cm^{-3}, which includes all of the actual hole concentrations of the three samples over the temperature range. Thus, the Lorenz numbers are nearly identical for all three samples at each temperature. Fig. S3*B* shows the reduced Fermi levels E_F/k_BT with regard to the valence band minimum in terms of the hole energy for the three samples. The hole concentrations obtained from the temperature-dependent Hall effect

measurements were used to calculate the Fermi levels. The reduced Fermi level steadily decreases with the temperature, but beyond ~550 K it becomes almost constant. This occurs because, at this temperature, the Σ-valley valence band becomes the lowest valence band such that the Fermi level is then referenced to the band minimum of the Σ-valleys. Because the band degeneracy of the Σ-valley is very high, the Fermi level does not change much with the variation of the hole concentration with the temperature.

The electronic thermal conductivity is obtained by the Wiedemann–Franz law using the Lorenz number from Eq. **S4** and adding the bipolar term (κ_{bi}) as

$$\kappa_e = L\sigma T + \kappa_{bi}, \qquad \textbf{[S5]}$$

where the bipolar electronic thermal conductivity is given by (6)

$$\kappa_{bi} = \frac{\sigma_e \sigma_h}{\sigma_e + \sigma_h}(S_e - S_h)^2 T, \qquad \textbf{[S6]}$$

where the subscripts e and h denote the partial contributions of the electrons and holes, respectively, to each quantity. The bipolar electronic thermal conductivity can be significantly large, particularly at high temperatures, even if the intrinsic carrier densities are much lower than the doping density because the Seebeck coefficients of the two types have opposite signs; they are added in Eq. **S6**. Also, κ_{bi} increases proportionally to the temperature.

The relaxation time is determined by several major scattering mechanisms in the bulk materials. Acoustic phonon deformation potential scattering, polar optical phonon scattering, and ionized impurity scattering are included in the calculations, but it was found that the acoustic phonon deformation potential scattering is the dominant scattering mechanism in bulk PbTe. In our nanostructured materials, however, the additional scattering mechanism of the grain boundary scattering can be very strong and increase the electrical resistivity quite significantly. Our electrical resistivity measurements confirm this; they are significantly higher than the calculated bulk values, as shown in Fig. 3*A*.

The hole concentrations were measured by the Hall effect measurements from room temperature to 780 K. These are plotted in Fig. S4 for the three samples. The data are quite substantially noisy because the electrical current used for the Hall effect measurements was limited to 100 mA by the Hall effect measurement system. Due to the large size and relatively low resistivity of the samples, the voltage signal was weak and the noise level was high. Despite the noisy data, the trend of the increasing hole concentration with an increase in the temperature is clearly shown for all three samples. Therefore, we were able to fit the temperature-dependent hole concentrations for the samples, shown as solid curves in Fig. S4. The AH sample had the lowest hole concentration (3.5×10^{19} cm^{-3}) compared with those of the QAH and QH samples (5.0×10^{19} cm^{-3} and 6.5×10^{19} cm^{-3}, respectively) at room temperature, but it increased more rapidly with the temperature compared with the other two samples above 600 K, reaching 6×10^{19} cm^{-3} at 780 K. The QAH and QH samples have similar hole concentrations of 1.09×10^{19} cm^{-3} and 1.05×10^{19} cm^{-3}, respectively, at 780 K according to the fitting result.

Simulation on the Lattice Thermal Conductivity. The thermal conductivity of the phonons is predicted using Callaway's model (7), which is calculated as

$$\kappa = \frac{k_B}{2\pi^2 \upsilon} \times \left(\frac{k_B T}{\hbar}\right)^3 \times \left\{ \int_0^{\theta/T} \frac{\tau_c x^4 e^x}{(e^x-1)^2} dx + \frac{\left[\int_0^{\theta/T} \frac{\tau_c}{\tau_N} \frac{x^4 e^x}{(e^x-1)^2} dx\right]^2}{\int_0^{\theta/T} \frac{1}{\tau_N}\left(1-\frac{\tau_c}{\tau_N}\right)\frac{x^4 e^x}{(e^x-1)^2} dx} \right\}, \qquad \textbf{[S7]}$$

where $\hbar$ is Planck's constant divided by 2π, x is the normalized frequency, and $\hbar\omega/k_B T$. υ, and θ are the speed of sound and the Debye temperature, respectively. Here, τ_N is the relaxation time due to normal phonon–phonon scattering, and τ_c is the combined relaxation time using Matthiessen's rule (8, 9), given as

$$\tau_c^{-1} = \tau_B^{-1} + \tau_U^{-1} + \tau_N^{-1} + \tau_A^{-1} + \tau_D^{-1} + \tau_{e-ph}^{-1} \qquad \textbf{[S8]}$$

expressed in terms of the grain boundary scattering τ_B, the Umklapp scattering τ_U, the alloy scattering τ_A, the scattering due to nanoparticles τ_D, and the electron–phonon scattering $\tau_{e\text{-}ph}$. The relaxation time expressions for normal, Umklapp, alloy and electron–phonon scattering are based on those found in the literature (10–13). The sizes of the grain boundaries were set to 100, 8, and 3.7 μm for the AH, QAH, and QH samples, respectively, based on the SEM images. In particular, for the electron–phonon scattering rate to be consistent with the power factor calculation, we considered the band convergence (14). The effective electron mass for the L valley is 0.15 m_e (m_e is the electron rest mass), which is the dominant valley at 300 K; at 560 K, this overlaps with the Σ-valley, which becomes the dominant valley at 800 K. The effective mass for the Σ-valley is 0.37 m_e. The scattering caused by nanoscale precipitates τ_D was approximated by scattering due to the nanoparticles (15). In this case, out of 2% Na-doped on PbTe, 0.5% Na was dissolved due to the solubility limit (16) and the remaining 1.5% was assumed to be precipitated in the form of Na_2Te with sizes of around 10, 7, and 2.4 nm diameter for the AH, QAH, and QH samples, respectively. We used (17) a Debye temperature of 136 K, the average sound velocity among different branches, a lattice constant of 6.46 Å, and a lattice anharmonic constant (18) of 65.

Lattice thermal conductivities of the QH, AH, and QAH samples with and without nanoparticles (NP) are shown in Fig. S5. It is clear in the figure that effects of NPs on the lattice thermal conductivities are evident in the QH but are not significant in the others. Interestingly, although the nanostructures occur in all three samples, QH, AH, and QAH, nanostructures only a few nanometers in diameter present in QH effectively reduced the lattice thermal conductivity. Based on this finding, we emphasize that nanostructures are not always effective in reducing the lattice thermal conductivity. They are the most effective when the spacing between them is smaller than the phonon mean-free paths of other scattering processes.

We performed sensitivity analysis on lattice thermal conductivity regarding the variation of sizes of nanoparticles and microsized grains in our samples (Fig. S6). As shown in the figure, the variation of micrograin sizes by ±10% affects the lattice thermal conductivity almost negligibly in all of the samples. On the other hand, the variation of nanoparticle sizes by ±10% varies the lattice thermal conductivity by 3 ~ 4% in the QH sample, and by less than 1% in the AH and QAH samples. This indicates that our analysis based on the room-temperature size distribution could still be valid at high temperatures

unless there is a significant variation of the size distribution by much larger than 10%. In addition, the largest variation of lattice thermal conductivity in the QH sample by the same degree of size variation further supports our conclusion that by the optimized synthesis process and conditions, the sizes of nanoparticles finally became small enough to effectively alter the lattice thermal conductivity in the Na-doped PbTe at high temperatures.

The Repeated Measurements on Thermoelectric Properties of the QH Samples. The repeated thermoelectric properties of the QH samples are presented in Fig. S7. Regarding the 13 measurements for 4 QH samples, some of the measurements were performed at Korea Electrotechnology Research Institute for corroboration purpose. Unusually low thermal conductivities of s2-2nd and s2-3rd were mainly due to the low thermal diffusivities. Fig. S8 shows the thermoelectric properties for QH while heating or cooling the sample.

1. Wang H, et al. (2013) Large enhancement in the thermoelectric properties of Pb0.98Na0.02Te by optimizing synthesis condition. *J Mater Chem A* 1:11269–11278.
2. Baram M, Kaplan WD (2008) Quantitative HRTEM analysis of FIB prepared specimens. *J Microsc* 232(3):395–405.
3. Blachnik R, Igel R (1974) Thermodynamic properties of IV-VI-compounds - lead - chalcogenides. *Z Naturforsch B* 29:625–629.
4. Ravich YI, Efimova BA, Smirnov IA (1970) *Semiconducting Lead Chalcogenides* (Plenum, New York).
5. Vineis CJ, et al. (2008) Carrier concentration and temperature dependence of the electronic transport properties of epitaxial PbTe and PbTe/PbSe nanodot superlattices. *Phys Rev B* 77(23):235202.
6. Nolas GS, Goldsmid HJ (2004) Thermal conductivity of semiconductors. *Thermal Conductivity: Theory, Properties, and Applications*, ed Tritt TM (Kluwer Academic, New York).
7. Callaway J (1959) Model for lattice thermal conductivity at low temperatures. *Phys Rev* 113(4):1046–1051.
8. Ashcroft NW, Mermin ND (1976) *Solid State Physics* (Holt, Rinehart and Winston, New York).
9. Tien CL, Majumdar A, Gerner FM (1998) *Microscale Energy Transport* (Taylor & Francis, Washington, DC).
10. Abeles B (1963) Lattice thermal conductivity of disordered semiconductor alloys at high temperatures. *Phys Rev* 131(5):1906–1911.
11. Minnich AJ, et al. (2009) Modeling study of thermoelectric SiGe nanocomposites. *Phys Rev B* 80(15):155327.
12. Morelli DT, Heremans JP, Slack GA (2002) Estimation of the isotope effect on the lattice thermal conductivity of group IV and group III-V semiconductors. *Phys Rev B* 66(19):195304.
13. Vining CB (1991) A model for the high temperature transport properties of heavily doped n-type silicon-germanium alloys. *J Appl Phys* 69(1):331–341.
14. Pei Y, et al. (2011) Convergence of electronic bands for high performance bulk thermoelectrics. *Nature* 473(7345):66–69.
15. Kim W, Majumdar A (2006) Phonon scattering cross section of polydispersed spherical nanoparticles. *J Appl Phys* 99:084306.
16. He J, et al. (2013) Role of sodium doping in lead chalcogenide thermoelectrics. *J Am Chem Soc* 135(12):4624–4627.
17. Lo SH, He JQ, Biswas K, Kanatzidis MG, Dravid VP (2012) Phonon scattering and thermal conductivity in p-type nanostructured PbTe-BaTe bulk thermoelectric materials. *Adv Funct Mater* 22(24):5175–5184.
18. Koh YK, Vineis CJ, Calawa SD, Walsh MP, Cahill DG (2009) Lattice thermal conductivity of nanostructured thermoelectric materials based on PbTe. *Appl Phys Lett* 94(15):153101.

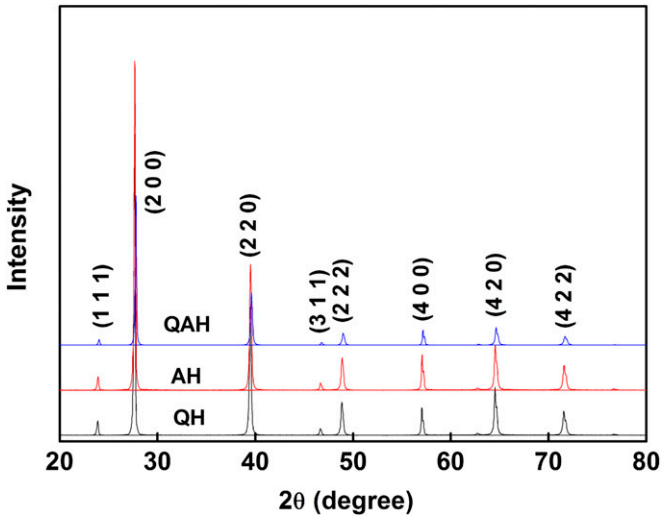

Fig. S1. XRD patterns of $Pb_{0.98}Na_{0.02}Te$ samples with different synthesis methods.

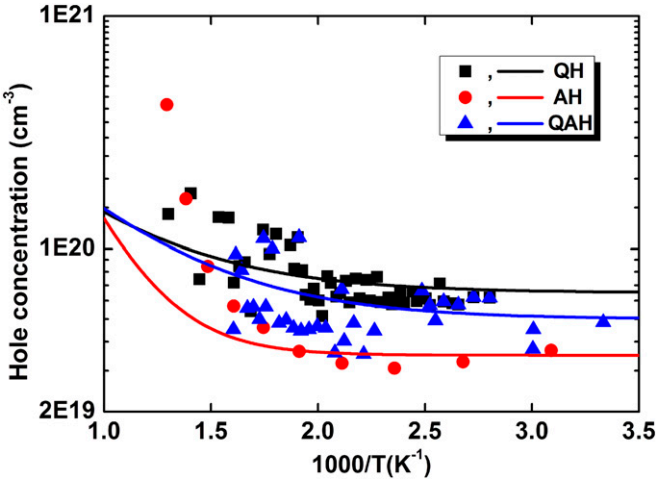

Fig. S2. Hall effect hole concentrations as a function of the reciprocal temperature (1,000/*T*) for the QH, AH, and QAH samples with fitting curves (solid lines).

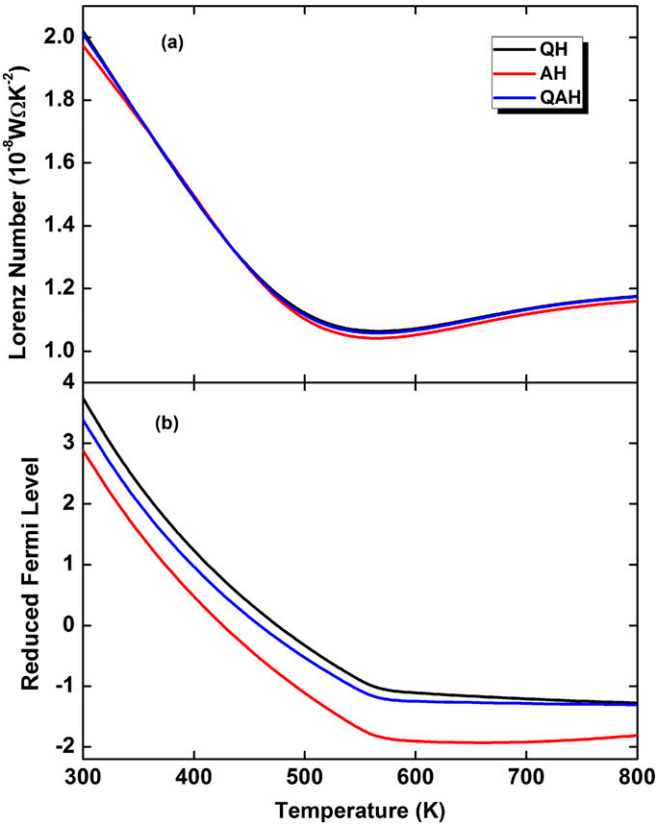

Fig. S3. Temperature dependence of (*A*) the Lorenz numbers and (*B*) the reduced Fermi levels for the QH, AH, and QAH samples.

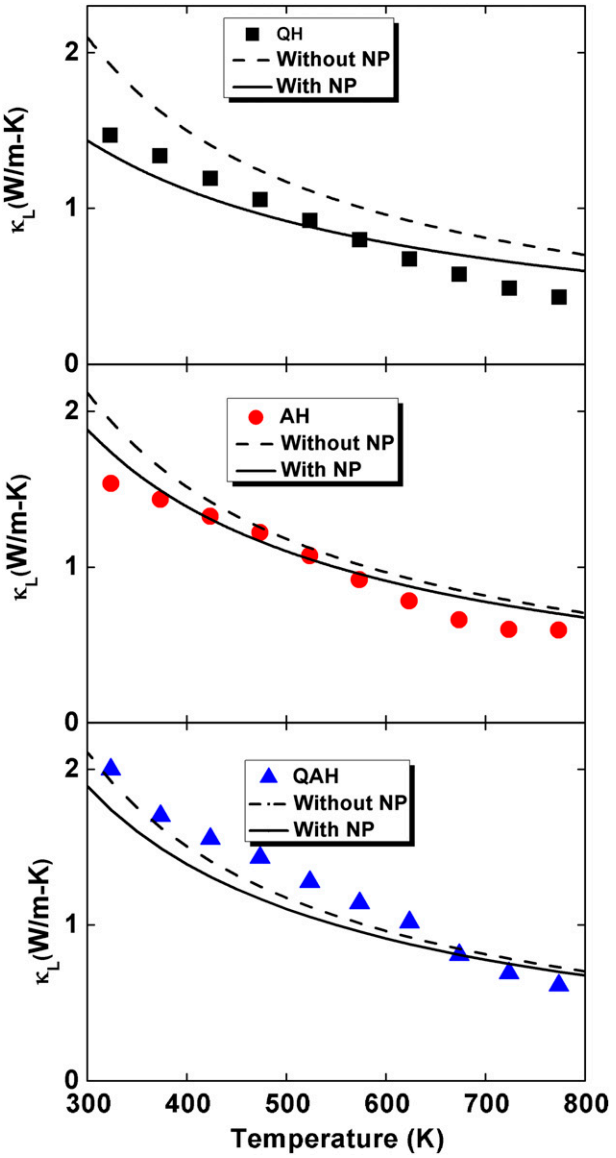

Fig. S4. Lattice thermal conductivities of the QH, AH, and QAH samples with and without NP.

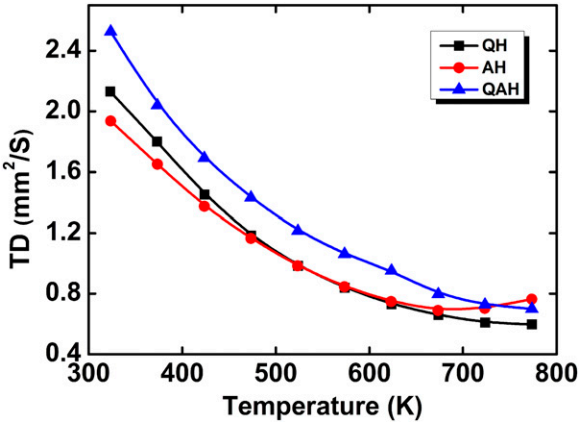

Fig. S5. Thermal diffusivities of the QH, AH, and QAH samples.

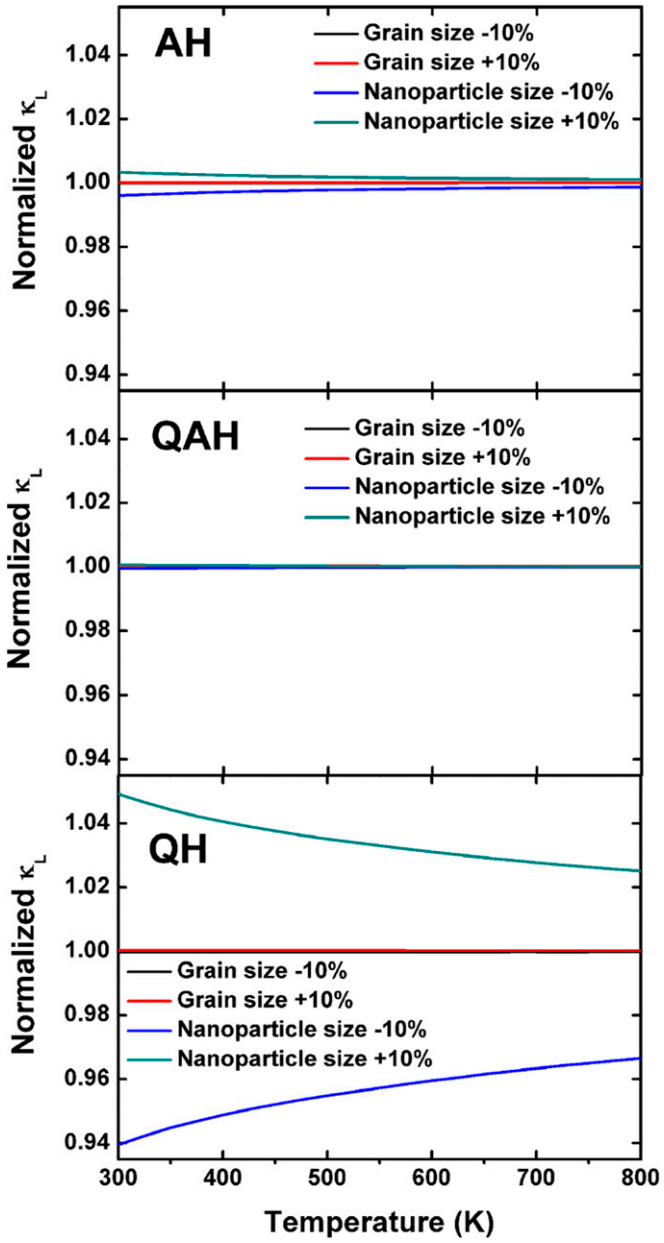

Fig. S6. Sensitivity analysis results for the QH, AH, and QAH samples at varying temperatures.

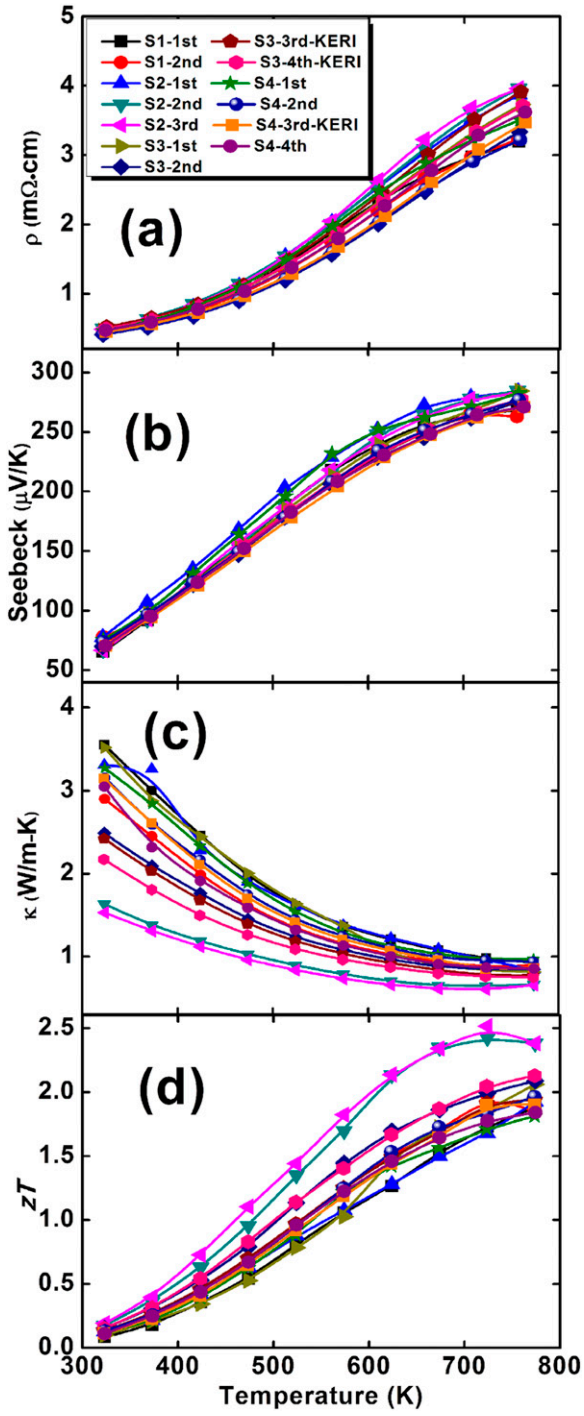

Fig. S7. Repeated measurements of thermoelectric properties for the four QH samples: (*A*) electrical resistivities, (*B*) Seebeck coefficients, (*C*) total thermal conductivities, and (*D*) the thermoelectric figures of merit.

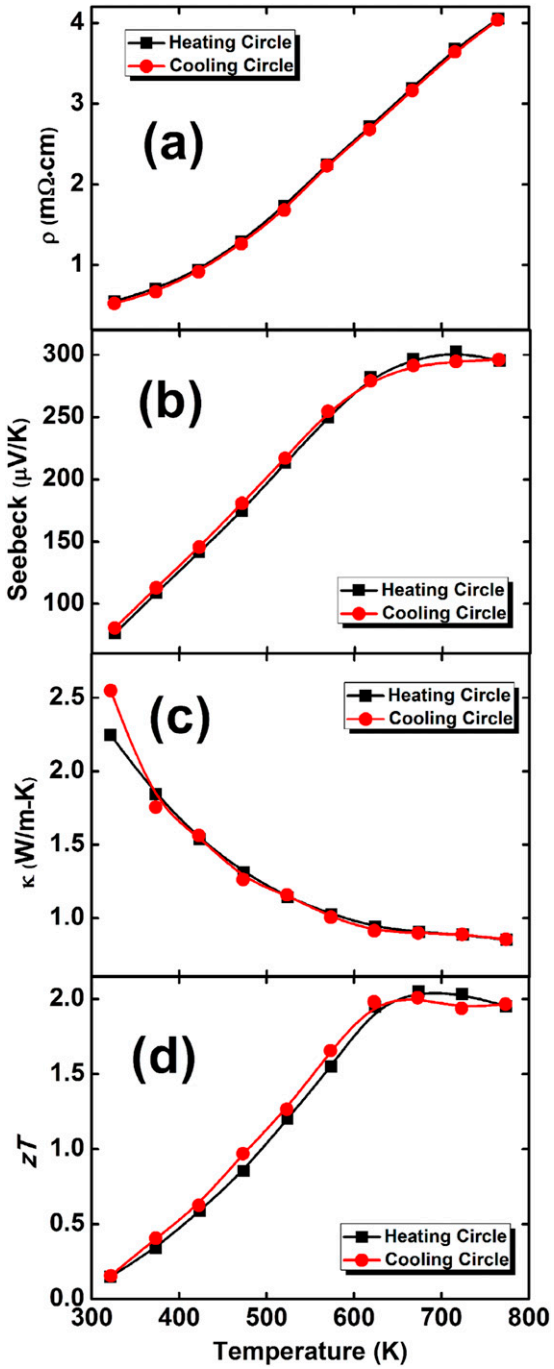

Fig. S8. Thermoelectric properties for QH while heating or cooling the sample; (*A*) electrical resistivities, (*B*) Seebeck coefficients, (*C*) total thermal conductivity, and (*D*) the thermoelectric figures of merit.

Table S1. Lattice constants, volumes, theoretical densities, and experimental densities for $Pb_{0.98}Na_{0.02}Te$ samples with different synthesis methods

Samples	a, Å	V, Å^3	Theoretical density, g/cm^3	Experimental density, g/cm^3
QH	6.456	269.09	8.176	8.174
AH	6.457	269.19	8.173	8.172
QAH	6.457	269.20	8.173	8.148